Fuel 416 (2026) 138521

Contents lists available at ScienceDirect

Fuel

journal homepage: www.elsevier.com/locate/fuel

Full Length Article

Amorphous high-entropy Co_3B-HEA: Enhanced $NaBH_4$ hydrolysis catalysis via multi-element synergy

Huaxia Zhou [a], Chenxi Shang [a], Tayirjan Taylor Isimjan [b,*], Xiulin Yang [a,*]

[a] Guangxi Key Laboratory of Low Carbon Energy Materials, School of Chemistry and Pharmaceutical Sciences, Guangxi Normal University, Guilin 541004, China
[b] Saudi Arabia Basic Industries Corporation (SABIC) at King Abdullah University of Science and Technology (KAUST), Thuwal 23955-6900, Saudi Arabia

ARTICLE INFO

Keywords:
Amorphous
Co_3B–HEA
High-entropy alloys
Electronic interaction
$NaBH_4$ hydrolysis

ABSTRACT

High-entropy materials, with their multi-element synergistic effects, offer abundant active sites, holding great promise for designing efficient catalysts for sodium borohydride ($NaBH_4$) hydrolysis. Herein, we for the first time synthesize a metal-rich amorphous high-entropy compound Co_3B–HEA via a hydrothermal-chemical reduction method, constructing a novel "high-entropy matrix-boride" composite catalytic system. Experimental results demonstrate that Co_3B–HEA achieves a maximum hydrogen generation rate (HGR) of 8539.2 mL min^{-1} g_{cat}^{-1} at 25 °C. Systematic characterizations reveal three key structural innovations: uniformly distributed multi-metallic active sites, a unique amorphous structure, and strong electronic interactions between Co_3B and the HEA matrix. Kinetic studies demonstrate zero-order reaction behavior with respect to $NaBH_4$ concentration and a low activation energy (47.24 kJ mol^{-1}), indicating enhanced reaction efficiency. Based on the Michaelis–Menten model, we propose a novel multi-element synergistic activation mechanism: Ru, Co, Fe, Ni, and Mo collectively activate BH_4^- and H_2O molecules, fundamentally boosting the $NaBH_4$ hydrolysis rate. Moreover, hydrogen generated from $NaBH_4$ hydrolysis by the Co_3B–HEA catalyst was used directly to drive a custom H_2-air fuel cell, successfully lighting up small light bulbs and demonstrating its potential for practical applications. This work offers a novel strategy for designing high-performance catalysts for hydrogen production and their practical energy utilization.

1. Introduction

In recent years, high-entropy alloys (HEA) have emerged as novel catalytic materials, demonstrating significant potential in fields such as water splitting, CO_2 reduction and dye degradation [1–3]. Current research on $NaBH_4$ hydrolysis hydrogen catalysts primarily focuses on single-metal (e.g., Co–B [4], Co@NHC [5]), bimetallic catalysts (e.g., PtCo/g-C_3N_4 [6], Co_2B–Fe_2B [7]), and trimetallic catalysts (e.g., Ru/Co–Sm_2O_3 [8], Co/$CuFe_2O_4$ [9]). Although these catalysts exhibit excellent activity, their performance is often constrained by the inherent limitations of atomic-level activity in metals [10]. To overcome these limitations, the incorporation of multiple components has emerged as a powerful strategy for enhancing the catalytic performance of metal-based systems. Compared to traditional metal composites, HEA represent a distinct class of multi-principal element alloys composed of five or more metallic elements [11]. Their unique advantages originate from four fundamental effects: the high entropy effect [12], the lattice distortion effect [13], the slow diffusion effect [14], and the mixed entropy effect [15]. These effects provide an effective pathway to address the aforementioned limitations: (1) Multi-element synergistic building of dual-functional activation sites for BH_4^- and H_2O, increasing reaction efficiency [16]; (2) Lattice distortion modifies the d orbital electron density at metal active sites, improving adsorption energy and reducing reaction energy barriers [17]. This synergistic advantage of "high activity–high stability" enables HEA to demonstrate exceptional application potential in the strongly alkaline environment of $NaBH_4$ hydrolysis, offering a novel strategy for designing high-performance hydrogen storage catalysts.

Recent studies indicate that amorphous catalysts, owing to the abundance of unsaturated coordination sites arising from their disordered atomic structure, exhibit superior catalytic activity to crystalline catalysts in the hydrolysis reaction of $NaBH_4$ [18]. Although HEA can generate synergistic multi-active sites through the combined effects of high entropy, lattice distortion, and sluggish diffusion, the majority of HEA are inherently crystalline and lack the electronic modulation benefits associated with borides. This structural constraint limits their catalytic performance to the intrinsic reactivity of constituent metal atoms, thereby impeding further enhancement of catalytic activity. Therefore,

* Corresponding authors.
E-mail addresses: isimjant@sabic.com (T.T. Isimjan), xlyang@gxnu.edu.cn (X. Yang).

https://doi.org/10.1016/j.fuel.2026.138521
Received 19 September 2025; Received in revised form 15 December 2025; Accepted 22 January 2026
Available online 27 January 2026

the incorporation of boron, especially derived from boron-rich metal borides (M_xB, $x > 2$), into high-entropy materials can further enhance their structural stability and catalytic performance [19]. The electron transfer from boron atoms to adjacent metal atoms increases the electron density in the d-orbitals of the metal sites, thereby improving the catalytic performance [20]. Transition metals Ru, Fe, Co, Ni, and Mo all exhibit significant activity in $NaBH_4$ hydrolysis. Combining base metals such as Co, Fe, Mo, and Ni with the noble metal Ru promotes electron transfer and elemental synergistic effects [17]. The unique interplay between the multiple elements on the surface of HEA nano-catalysts and thus synergistic effect (often referred to as the cocktail effect) can create a diverse range of active sites with optimal binding energies for reactants, intermediates, and products [21]. For example, recent theoretical calculations have validated a pronounced synergistic effect arising from the multi-element composition of PtFeCoNiCu HEA nanoparticles [14]. Consequently, introducing B into high-entropy systems to construct amorphous porous nanoparticle structures can significantly enhance. However, to the best of our knowledge, few works has focused on the HEA catalyzing the $NaBH_4$ hydrolytic.

Based on the aforementioned design principles, this study pioneered the combination of borides with high-entropy materials through a hydrothermal-chemical reduction approach to synthesize an amorphous high-entropy Co_3B-HEA catalyst, which substantially enhances the hydrolysis efficiency of sodium borohydride. The synthesized catalyst's crystallinity, microstructure, porosity, and chemical states were investigated using a wide range of characterization methods, such as X-ray diffraction (XRD), scanning electron microscopy (SEM), Brunauer-Emmett-Teller (BET) surface area analysis, zeta potential measurements, and X-ray photoelectron spectroscopy (XPS). According to experimental data, the amorphous Co_3B–HEA catalyst exhibits high catalytic efficiency and significantly enhanced performance in the $NaBH_4$ hydrolytic. Furthermore, by integrating insights from previous studies with the Michaelis-Menten kinetic model, we propose a plausible reaction mechanism, thereby providing a theoretical basis for understanding the enhanced catalytic performance.

2. Experimental section

2.1. Materials

Ruthenium(III) chloride hydrate ($RuCl_3{\cdot}xH_2O$, 99 %, Innochem), cobalt(II) nitrate hexahydrate ($Co(NO_3)_2{\cdot}6H_2O$, 99.0 %, Aladdin), iron (III) nitrate nonahydrate ($Fe(NO_3)_3{\cdot}9H_2O$, 99.0 %, Aladdin), nickel(II) nitrate hexahydrate ($Ni(NO_3)_2{\cdot}6H_2O$, ≥98 %, Aladdin), ammonium molybdate tetrahydrate ($(NH_4)_6Mo_7O_{24}{\cdot}4H_2O$, 99.0 %, Aladdin), cobalt (II) chloride hexahydrate ($CoCl_2{\cdot}6H_2O$, ≥99.0 %, Aladdin), 2,5-dihydroxyterephthalic acid (DOBDC), N, N-Dimethylformamide (DMF), sodium borohydride ($NaBH_4$, ≥98.0 %, Sinopharm Group), sodium hydroxide (NaOH, ≥96.0 %, Aladdin), anhydrous ethanol. All reagents are commercially available and can be used directly without further purification. All aqueous solutions were prepared with deionized water.

2.2. Ingredient design

In this work, Ru-containing high-entropy amorphous alloys were as boronization precursors for fabricating nanoporous alloy catalysts. Sufficient amorphous formation capability and unique SEP of constituent elements were critical. Additionally, Ru content in the alloy should not be excessively high to ensure cost-effectiveness. Based on this principle, transition metals Co, Fe, Ni, Mo, and metalloids B were selected for alloying with Ru. Within this alloy system, the atomic sizes of Ru, Co, Fe, Ni, Mo and B are 0.133 nm, 0.125 nm, 0.124 nm, 0.125 nm, 0.139 nm, and 0.098 nm, respectively. The mixed enthalpy between metal (Ru, Co, Fe, Ni, Mo)-metalloid (B) atom pairs ranges from −24 to −49 kJ mol^{-1} (**Fig. S1a**). The significant size mismatch between atomic pairs, coupled with the large negative mixing enthalpy, jointly promotes the formation of the amorphous phase. On the other hand, the standard electrode potentials of Ru, Co, Fe, Ni, Mo and B (relative to the standard hydrogen electrode SHE) are 445 mV, −277 mV, −440 mV, −230 mV, −220 mV, and − 870 mV (**Fig. S1b**). The substantial standard potential differences among constituent elements render high-entropy alloys ideal precursors for fabricating nanoporous alloys [18]. The resulting five-component system exhibits high mixed entropy and thermodynamic stability, effectively suppressing agglomerative oxidation through composite structure formation with borides.

2.3. Synthesis of HEA

The synthesis of RuCoFeNiMo started with the dissolution of 0.25 mmol of $RuCl_3{\cdot}xH_2O$, 0.25 mmol of $Co(NO_3)_2{\cdot}6H_2O$, 0.25 mmol of $Fe(NO_3)_3{\cdot}9H_2O$, 0.25 mmol of $Ni(NO_3)_2{\cdot}6H_2O$, 0.075 mmol of $(NH_4)_6Mo_7O_{24}{\cdot}4H_2O$, and 1.5 mmol of 2,5-dihydroxy terephthalic acid in the mixture of 22.5 mL of DMF, 3 mL of anhydrous ethanol, and 3 mL of DI water. Then, the mixture was sonicated for at least 60 min. Subsequently, the mixture was immediately transferred into a 100 mL autoclave and then heated to 120 °C for 48 h. The synthesized RuCoFeNiMo precursor was washed with ultrapure DI water, DMF, and EtOH in sequence several times and dried for 12 h at 70 °C. (In the subsequent synthesis sections of this paper, when RuCoFeNiMo are used as carriers, we denote them by HEA).

2.4. Synthesis of Co_3B−HEA

At room temperature, 0.02 g of HEA and 0.08 g of $CoCl_2{\cdot}6H_2O$ in a beaker containing 30 mL of ethanol. Stir at 600 rpm for 1 h. After adding 5 mL of 5 % $NaBH_4$ solution, continue stirring for 30 min. The precipitated black particles were repeatedly washed with water and ethanol, then dried at 70°C. This material was designated Co_3B−HEA. The Co_3B catalyst was prepared following the same procedure, omitting only the HEA step.

3. Results and Discussion

3.1. Synthesis strategy and Microstructural analysis

The Co_3B–HEA catalyst was synthesized by combining hydrothermal synthesis with a subsequent chemical reduction strategy. The stepwise synthesis procedure is illustrated in Fig. 1a. Initially, the HEA was prepared via a hydrothermal method by coordinating Ru^{3+}, Co^{2+}, Fe^{3+}, Ni^{2+}, and Mo^{6+} ions with the organic ligand 2,5-dihydroxy terephthalic acid (DOBDC), resulting in the formation of a multi-metallic complex. This HEA was subsequently used as a substrate for cobalt deposition by impregnation with $CoCl_2{\cdot}6H_2O$. Finally, the Co^{2+}–HEA precursor was chemically reduced using a 5 % $NaBH_4$ solution to introduce B, obtaining the Co_3B–HEA catalyst.

The HEA precursor exhibited a homogeneous spherical shape, according to scanning electron microscopy (SEM) (Fig. 2a). The Co^{2+}–HEA precursor changed into evenly distributed porous nanoparticles after being impregnated with $CoCl_2{\cdot}6H_2O$ for an hour and then reduced with $NaBH_4$ (Fig. 2b). The hydrolysis of sodium borohydride can be significantly facilitated by the porous structure of the nanoparticles, which exposes a large number of active sites, enhances atomic utilization efficiency, promotes electrolyte infiltration, and accelerates ion and mass transport [22,23]. Additional, SEM images (**Fig. S2**) show that Co_3B also exhibits irregular porous nanoparticles. TEM analysis further confirmed the morphological characteristics of the Co_3B–HEA catalyst (Fig. 2c). The lack of distinct lattice fringes in the high-resolution TEM (HR-TEM) picture confirms that Co_3B–HEA is amorphous (Fig. 2d). This amorphous structure is further substantiated by the diffuse and continuous halo ring observed in the selected area electron diffraction (SAED) pattern (inset in Fig. 2d) [24]. Amorphous compounds often exhibit loosely packed atomic arrangements and highly disordered structures, which might

IVB	VB	VIB	VIIB	VIIIB			IB
Ti	V	Cr	Mn	Fe	Co	Ni	Cu
Zr	Nb	Mo	Tc	Ru	Rh	Pd	Ag
Hf	Ta	W	Re	Os	Ir	Pt	Au

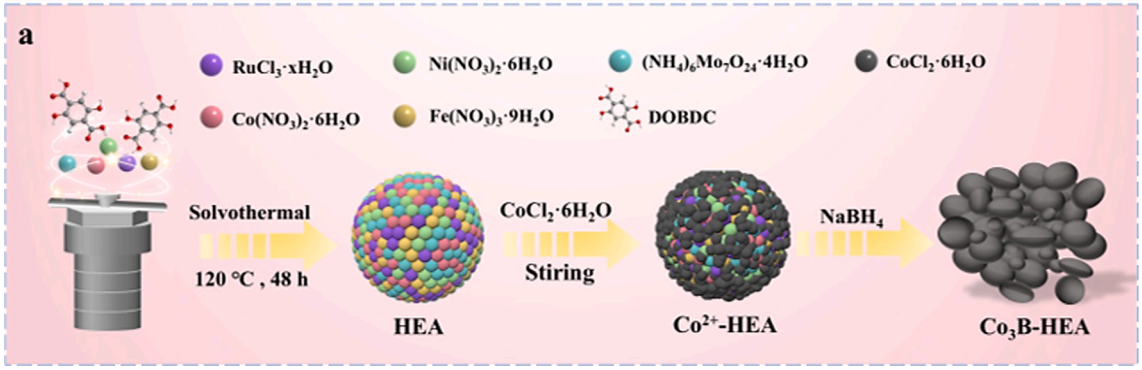

Fig. 1. (a) Schematic protocol of the synthesis strategy for Co_3B–HEA.

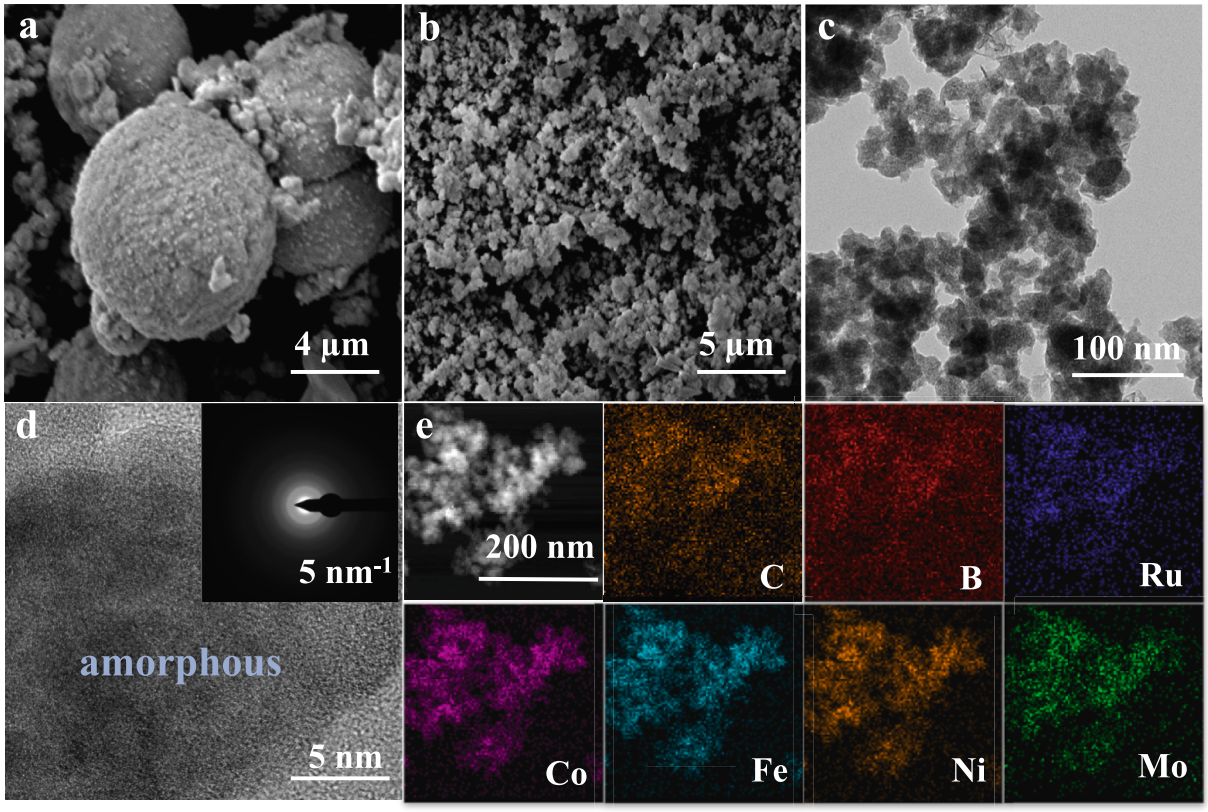

Fig. 2. (a) SEM image of HEA. (b) SEM image of Co_3B–HEA. (c) TEM image of Co_3B-HEA. (d) HR-TEM image of Co_3B-HEA. (e) HAADF-TEM image and elemental mappings of Co_3B–HEA and the corresponding elemental mappings (C, B, Ru, Co, Fe, Ni, Mo).

facilitate quick ion diffusion paths in the $NaBH_4$ hydrolytic [25]. Furthermore, elemental mapping and energy-dispersive X-ray spectroscopy (EDS) analysis demonstrate the uniform distribution of Ru, Co, Fe, Ni, Mo, and B throughout the material (Fig. 2e and **Table S1**). This homogeneous elemental distribution is expected to promote synergistic interactions among the various metal components, contributing to improved catalytic performance [26].

The structural characteristics of the catalyst were analyzed using X-

ray powder diffraction (XRD). As shown in Fig. 3a, the precursor HEA exhibits two distinct diffraction peaks at approximately 43.9° and 50.9°, corresponding to the (111) and (200) planes of a face-centered cubic (FCC) structure, thereby confirming the successful synthesis of the HEA phase [27,28]. However, due to the predominant amorphous nature of HEA, the diffraction peaks are not very pronounced. No diffraction peaks from metal oxides, or other impurity phases were detected, confirming the absence of significant phase separation in the system. Fourier-transform infrared spectroscopy (FT-IR) further confirmed the chemical composition of the precursor HEA, as shown in **Fig. S4**. The XRD pattern of the Co_3B–HEA sample (Fig. 3a) shows weak diffraction peaks that correspond to the Co_3B phase (JCPDS: 12–0443), demonstrating that the Co_3B–HEA compound is amorphous or low-crystalline. Additionally, a faint diffraction peak of the precursor HEA remains at 43.9°, confirming the successful synthesis of Co_3B on the HEA phase. The reduced crystallinity may lead to the presence of more active sites and could facilitate charge transfer [29]. The high-resolution TEM research supports this conclusion. This low crystallinity can be attributed to the substantial volume expansion occurring during the reduction of sodium borohydride, which reduces crystallinity and hinders the formation of distinct diffraction peak [30]. Furthermore, the X-ray diffraction patterns of pure Co_3B also exhibit significant differences from typical reference spectra (**Fig. S5**). Fig. 3b shows the relationship between the measured elemental composition and the calculated mixing entropy of the HEA. The elemental content falls within the range of 5 % to 35 %, satisfying the compositional criteria for HEA. Furthermore, the calculated mixing entropy (ΔS_{mix}), based on ICP–MS data (Table 1), is 12.34 — well within the HEA range of 11 to 19.5 — supporting the classification of the precursor ($Ru_{0.15}Co_{0.21}Fe_{0.11}Ni_{0.20}Mo_{0.19}$) as a high-entropy alloy rather than a medium-entropy alloy [10,31–33]. Additionally, the composition of the Co_3B–HEA product was also successfully determined (Table 1). Electron paramagnetic resonance (EPR) spectroscopy was used to investigate the presence of structural defects

Table 1
Inductive coupled plasma mass spectroscopy (ICP-MS) results of Co_3B–HEA.

Catalysts	Ru (wt. %)	Co (wt. %)	Fe (wt. %)	Ni (wt. %)	Mo (wt. %)
HEA	15.44	21.29	11.42	20.64	19.71
Co_3B-HEA	10.93	42.86	7.92	14.22	13.08
Co_3B-HEA -5^{th}	5.67	35.98	6.22	10.44	9.22

Note: The catalyst sample of 2.0 mg was weighed and dissolved in 8 mL aqua regia solution, followed by taking 80 μL solution to 100 mL volumetric flask with a pipette and diluted to 200 μg L^{-1} before ICP testing. The standard solution of Ru, Co, Fe, Ni, Mo was purchased from commercial company and used directly.

(Fig. 3c) [34]. Compared to the reference sample, Co_3B–HEA exhibits a stronger EPR signal (g = 2.14), which is attributed to a higher concentration of cobalt ion defects. These defects enhance electrical conductivity by modulating the electronic structure and promoting efficient charge transfer, thereby significantly improving catalytic performance.

The N_2 absorption/desorption isotherm of the Co_3B–HEA is shown in Fig. 3d, which features IV isothermal curves, forming an H_3 hysteresis loop, indicating the presence of mesopores. The N_2 adsorption/desorption measurements reveal that the Brunauer-Emmett-Teller (BET) surface area of Co_3B–HEA is 63.04 m^2 g^{-1}, with a pore size of 20.70 nm, substantially larger than that of the precursor HEA (Fig. 3d and **Fig. S6**). The enhanced surface area and mesoporous architecture contribute to a higher density of catalytically active surface sites, which is beneficial for improving catalytic performance [35,36]. The contact angle, which serves as a critical parameter for assessing surface hydrophilicity [37], was also measured. Co_3B–HEA exhibited a contact angle of 10.1°, significantly lower than that of the comparison sample, indicating enhanced interaction between the catalyst surface and hydroxyl groups. This result highlights the synergistic interaction between Co_3B and the HEA substrate, which plays a pivotal role in enhancing catalytic performance (Fig. 3e). Zeta potential measurements were conducted to

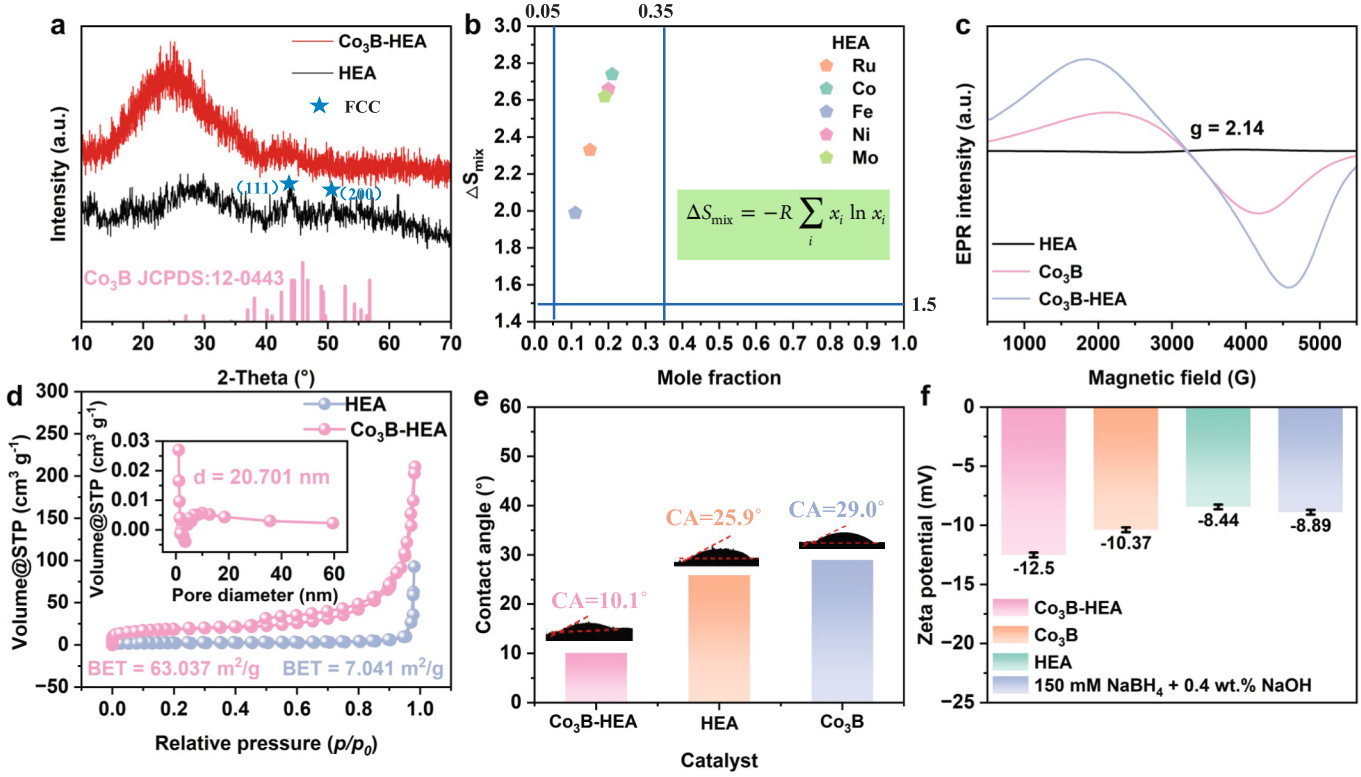

Fig. 3. (a) XRD pattern of HEA and Co_3B–HEA. (b) Calculated configurational entropy of HEA samples. The molar fractions of each element are derived from ICP-MS data. (c) EPR spectra of different catalysts. (d) N_2 adsorption–desorption isotherms, with insets showing the corresponding pore size distributions of Co_3B–HEA and HEA. (e) Bubble contact angle images of different catalysts. (f) Zeta potential of different catalysts in $NaBH_4$ solution.

examine the effects of a mixed solution (150 mmol/L $NaBH_4$ + 0.4 wt% NaOH) on the surface potentials of the catalysts shown in Fig. 3f, Co_3B-HEA exhibited optimized adsorption of OH^-/BH_4^-, with a higher negative potential of − 12.5 mV than Co_3B and HEA, suggesting a stronger electrostatic adsorption toward negatively charged BH_4^- ions. This property is particularly advantageous for $NaBH_4$ hydrolysis, where enhanced ion adsorption plays a critical role in boosting catalytic efficiency [38]. Finally, thermogravimetric analysis (TGA) and differential thermogravimetric analysis (DTG) were used to assess the thermal stability of the synthesized catalysts, as shown in **Fig. S7**. The total weight loss for HEA and Co_3B–HEA was found to be 44.85 % and 19.73 %, respectively, demonstrating the superior thermal stability of the Co_3B–HEA catalyst.

The electronic states and surface composition of the Co_3B–HEA catalyst were comprehensively analyzed using X-ray photoelectron spectroscopy (XPS). The survey spectra confirmed the presence of Ru, Co, Fe, Ni, Mo, and B, which is consistent with the elemental mapping results (**Fig. S8**). High-resolution XPS analysis of the C 1*s* region was performed using standard peak assignments for C−C (284.80 eV), C−O (286.20 eV), and C=O (288.50 eV), as shown in Fig. 4a [39]. The Ru 3*d* XPS spectrum was deconvoluted into two peaks at 281.44 eV and 282.21 eV, corresponding to metallic Ru and RuO_2, respectively, confirming the presence of metallic Ru in the catalyst (Fig. 4a) [40]. Compared to HEA, the Ru peak in Co_3B–HEA showed a 0.29 eV negative shift. As shown in Fig. 4b, the high-resolution Co 2*p* spectrum of Co_3B–HEA was fitted to components corresponding to Co–B (776.02 eV), Co^{3+} (780.74 eV), Co^{2+} (782.48 eV), and associated satellite peaks [41]. These results confirm that both Co^{2+} and Co^{3+} species coexist in the catalyst structure [42]. Notably, compared to the precursor HEA, the target sample Co_3B–HEA exhibits a Co–B peak, indicating the successful incorporation of boron, which enhances the structural stability and catalytic activity of these materials [19]. Fig. 4c shows the high-resolution Fe 2*p* spectrum, which was deconvoluted into Fe^{2+} (711.76 eV), Fe^{3+} (714.49 eV), and satellite peaks [43,44]. Compared to HEA, the Fe^{2+} peak in Co_3B–HEA showed a 0.54 eV positive shift. Similarly, the high-resolution Ni 2*p* spectrum in Fig. 4d revealed Ni^{2+} peaks at 856.05 eV and 873.52 eV along with corresponding satellite peaks [45]; Ni^{2+} also exhibited a 0.01 eV positive shift relative to HEA. In Fig. 4e, the Mo 3*d* spectrum was fitted into Mo^{4+} (231.35/234.35 eV) and Mo^{6+} (232.42/235.54 eV) components [46], with a 0.35 eV positive shift in the Mo^{4+} peak compared to HEA. These observed shifts in binding energy for Ru 3*d*, Co 2*p*, Fe 2*p*, Ni 2*p*, and Mo 3*d* indicate strong electronic interactions among the metal components within the HEA matrix after the introduction of boron. Specifically, the increases in binding energy suggest that Co, Ni, Fe, and Mo serve as electron donors [47], while Ru is likely to act as an electron acceptor [48]. This redistribution of electrons effectively reduces the kinetic barrier of the hydrolysis reaction by promoting the nucleophilic attack of water molecules [49]. The B 1*s* spectra for all samples show a peak at 191.86 eV, corresponding to B–O bonds. In Co_3B–HEA, a distinct peak observed at 187.27 eV is attributed to M−B bonding (Fig. 4f), which is shifted by approximately 0.27 eV from elemental boron (187.00 eV). This change indicates that electrons are transferred from the boron atoms in the alloy to the empty orbitals of transition metals (Co, Fe, Ni, and Mo), which causes an electron shortage in boron and enrichment of the metal centers. These results demonstrate that each metal element in the catalyst has changing valence states (valence state oscillation) [50], which can improve charge carrier mobility, alter the density of the electron cloud, and eventually lead to better catalytic performance. Moreover, the modified binding energies and rearranged electron distributions in high-entropy alloy systems enhance reaction kinetics, promote effective electron transfer throughout the catalytic process, and effectively reduce the reaction

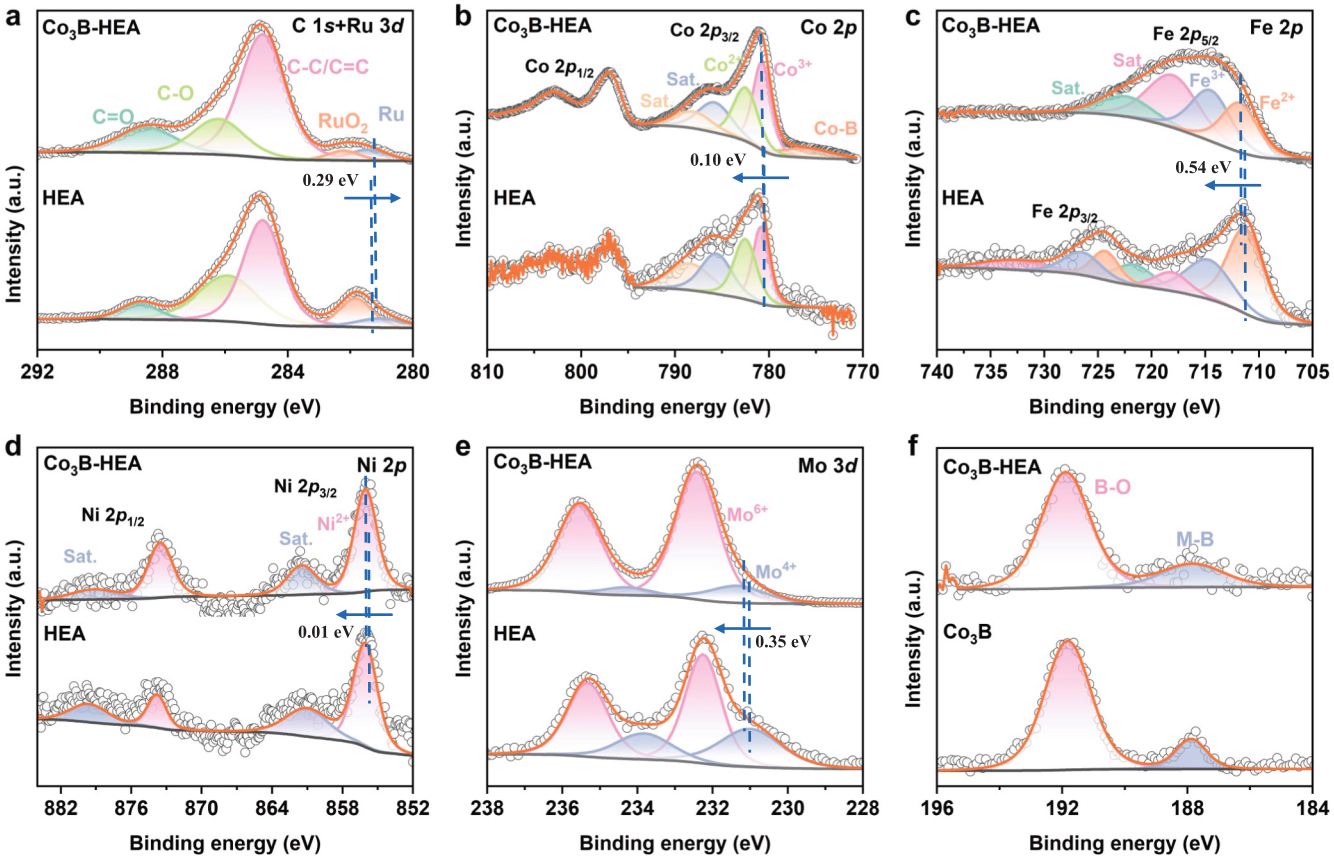

Fig. 4. High-resolution XPS spectra of Co_3B−HEA, HEA, and Co_3B for (a) C 1*s* + Ru 3*d*, (b) Co 2*p*, (c) Fe 2*p*, (d) Ni 2*p*, (e) Mo 3*d*, and (f) B 1*s*.

energy barrier for hydrolysis reactions [51].

3.2. Catalytic hydrolysis performance analysis

Hydrogen gas produced by the $NaBH_4$ hydrolytic in an alkaline media at 25 °C was quantified using the drainage technique (**Fig. S9**). It was observed that 150 mM $NaBH_4$ undergoes self-hydrolysis in aqueous solution even in the absence of a catalyst (**Fig. S10a**). To suppress this self-hydrolysis and achieve controlled reaction kinetics, NaOH was introduced as a stabilizer. Experimental results indicated that the addition of 0.4 wt% NaOH significantly reduced self-hydrolysis, with only negligible hydrogen release (**Fig. S10b**). A preliminary study was conducted to compare the catalytic hydrolysis performance of $NaBH_4$ using different catalysts, including Co_3B–HEA, Co_3B, and HEA. Among these, Co_3B–HEA demonstrated the most rapid hydrogen evolution kinetics, achieving a hydrogen generation rate (HGR) of 8539.2 mL min^{-1} g_{cat}^{-1}, significantly outperforming the other catalysts (Figs. 5a and 5b). This finding highlights the significant role played by the unique electronic structure and surface-active sites resulting from the synergistic interaction between Co_3B and the multi-metallic HEA matrix [52]. The amorphous nature of the catalyst and the rearrangement of electrons also accelerate the hydrogen release process. Furthermore, to elucidate the roles of individual metal elements within the catalytic system, single-metal-absence experiments were conducted (**Fig. S10**). Results indicate that the absence of either Ru or Co leads to an order-of-magnitude decrease in catalytic performance, confirming both as core components essential for sustaining high catalytic activity. Mechanistic studies reveal that Ru sites preferentially adsorb BH_4^- due to edge electron enrichment, thereby regulating the system's electron density [8]. Co sites strongly adsorb OH^-, promoting water molecule adsorption and O–H bond cleavage [53]. The absence of Fe, Ni, or Mo also causes significant performance degradation, as these elements synergistically regulate activity by promoting electron transfer and enhancing electron density at active sites [54–56]. Thus, the loss of any single element disrupts the synergistic "activity-regulation-stability" network, leading to substantial performance decline.

To further optimize catalytic performance, the effect of varying the mass ratio of Co to HEA during catalyst synthesis was investigated (Figs. 5a and 5b). The optimal HGR of 8539.2 mL min^{-1} g_{cat}^{-1} was obtained at a Co:HEA molar ratio of 2:1. However, increasing the cobalt ion concentration beyond this optimal ratio led to a gradual decline in catalytic activity. This decrease is attributed to nanoparticle aggregation at higher cobalt concentrations, which reduces the number of accessible active sites, thereby diminishing catalytic efficiency [30]. Furthermore, the effect of catalyst dosage (ranging from 5 mg to 20 mg) on HGR was investigated (Figs. 5c and 5d). The results revealed that 10 mg of Co_3B–HEA yielded the highest HGR. However, increasing the catalyst mass to 20 mg led to a significant decline in performance. This decrease

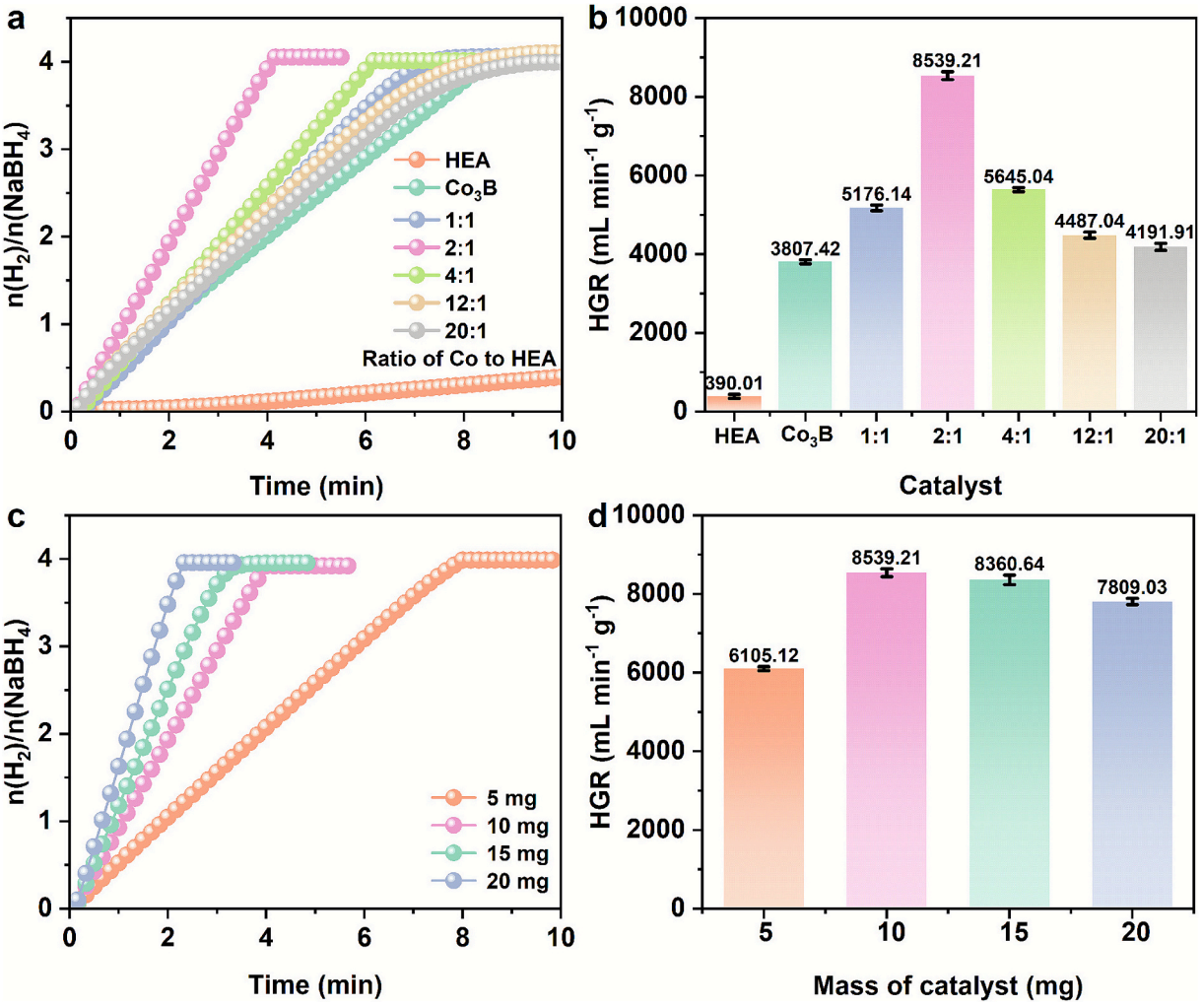

Fig. 5. (a) The equivalent H_2 per mole of sodium borohydride versus time with different catalysts and (b) the corresponding HGR values. (c) The equivalent H_2 per mole of sodium borohydride versus time with different masses of catalyst and (d) the corresponding HGR values. All tests were performed in 150 mM $NaBH_4$ + 0.4 wt % NaOH solution.

is probably the result of the solution's increased viscosity, which prevents the by-product $NaBO_2$ from diffusing effectively. The deposition of $NaBO_2$ on the catalyst surface may impede reactant interaction and reduce catalytic activity by blocking active sites [57,58].

See Fig. 6a shows that the hydrogen generation rate varies very little when the NaOH concentration is increased from 0 wt% to 0.8 wt%. This observation aligns with previous studies and confirms the remarkable stability of $NaBH_4$ in alkaline conditions. Additionally, we investigated the influence of $NaBH_4$ concentration on the hydrolysis reaction rate (Fig. 6b). The plot of ln(rate) against ln([$NaBH_4$]) is shown in the inset of Figs. 6b, and a slope of 0.068 was found. This nearly zero slope shows that the hydrolysis reaction catalyzed by Co_3B–HEA has zero-order kinetics and is unaffected by the concentration of $NaBH_4$ [59]. To evaluate the thermal dependence of the catalytic reaction, hydrolysis tests were carried out at different temperatures (298, 303, 308, 313, and 318 K) while keeping the concentrations of the Co_3B−HEA catalyst and alkaline $NaBH_4$ solution constant (Fig. 6c and **Fig. S11**). The results indicated that the hydrogen generation rate increased significantly with temperature and exhibited an approximately linear relationship with reaction time at each tested temperature (**Table S2-3)** [60]. Co_3B−HEA and Co_3B were shown to have apparent activation energies (E_a) of 47.24 and 52.02 kJ/mol, respectively, as determined from the Arrhenius plots. Among these, Co_3B−HEA exhibited the lowest activation energy, highlighting its superior catalytic efficiency and significantly lower than the values reported for some non-noble or noble mental catalysts in previous literature (**Table S4)**. This improvement can be attributed to a high density of surface-active sites, synergistic interactions among the multimetallic components, and the redistribution of electronic structures, which collectively facilitate electron transfer and enhance reactant activation [30].

The stability of a catalyst is a crucial factor in determining its suitability for large-scale hydrogen production via $NaBH_4$ hydrolysis, in addition to its catalytic activity. Experimental results indicate that the Co_3B–HEA catalyst requires only about 4.1, 5.0, 6.0, 6.9, and 7.8 min to complete the reaction for the consecutive five runs (Figs. 6e and 6f), respectively. To elucidate the reasons for this performance decline, the Co_3B–HEA catalyst after five catalytic cycles was thoroughly characterized using XRD (**Fig. S12**), SEM, XPS, and ICP-MS. SEM analysis revealed surface aggregation on the catalyst after repeated use (**Fig. S13**), suggesting morphological changes that may hinder reactivity. XPS analysis confirmed the continued presence of Ru, Co, Fe, Ni, Mo, and B (**Fig. S14**), with no significant compositional changes before and after cycling. Furthermore, high-resolution XPS spectra of C 1*s* + Ru 3*d*, Co 2*p*, Fe 2*p*, Ni 2*p*, Mo 3*d*, and B 1*s* showed no notable shifts, indicating that the chemical states of the active components remained largely stable throughout the cycling process (**Fig. S15**). However, ICP–MS analysis (Table 1) revealed a gradual decline in the overall metal content after five cycles. This loss may be due to minor leaching or peeling of metal components during the reaction, which results in a decrease in the number of catalytically active sites. Furthermore, the formation of by-products such as $NaBO_2$ during hydrolysis may cause physical blockage of these active sites, thereby further contributing to the observed decline in catalytic performance [8,57,61].

As discussed above, the Co_3B–HEA catalyst exhibits outstanding catalytic activity, primarily due to its unique amorphous structure, multicomponent composition, and the strong electronic interactions among its constituent elements. Building on the experimental findings and applying the Michaelis–Menten kinetic model, we propose a plausible reaction mechanism for $NaBH_4$ hydrolysis leading to hydrogen (H_2) generation (Fig. 7a). According to previous studies, BH_4^- ions preferentially adsorb onto the Ru sites present on the surface of Co_3B–HEA [53]. Furthermore, to investigate the adsorption sites for water molecules, the zeta potential of the single-metal catalysts in aqueous solutions were measured (**Fig. S16**). Notably, the zeta potential of Co_3B/Co–BDC was significantly more negative than those of Co_3B/Fe–BDC, Co_3B/Ni–BDC, and Co_3B/Mo–BDC, indicating a stronger electrostatic attraction for

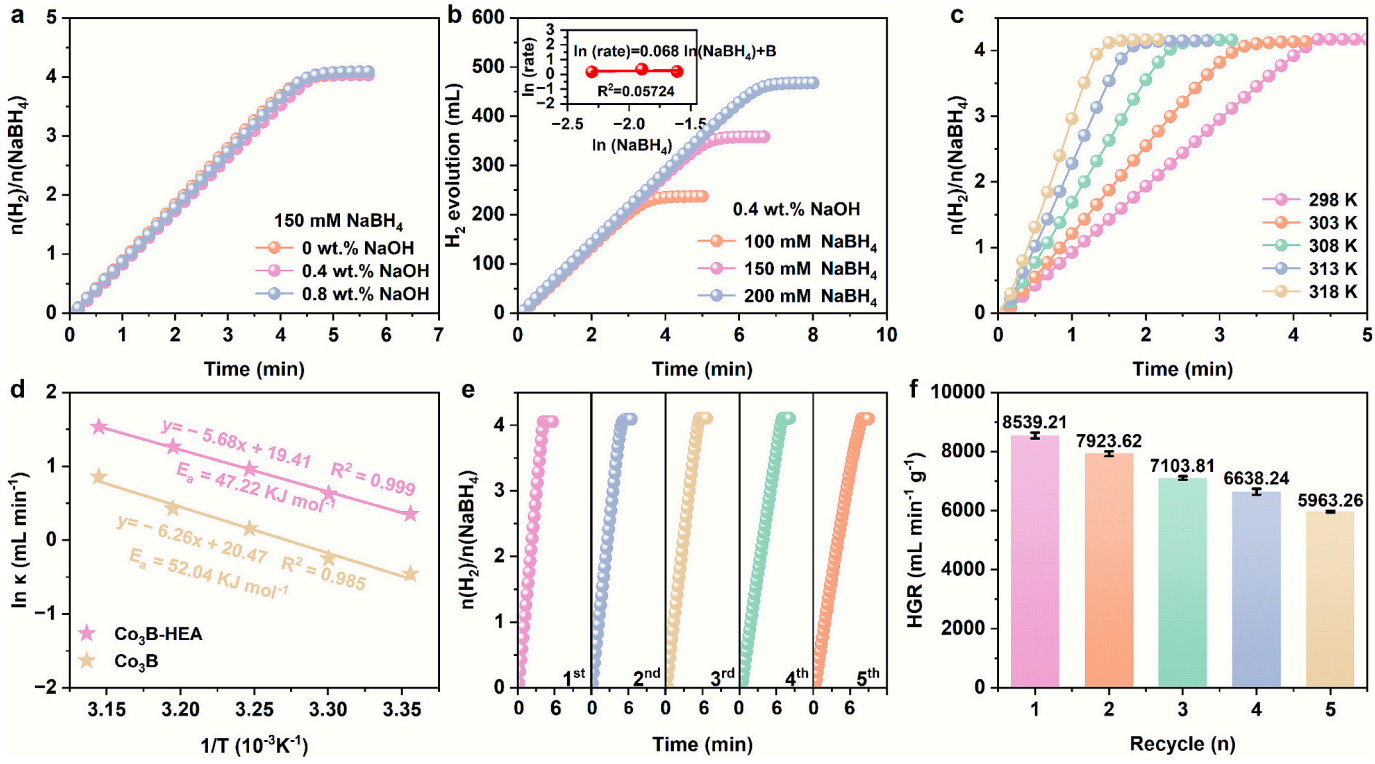

Fig. 6. (a) Effect of different NaOH contents on the HGR of the Co_3B−HEA at the same $NaBH_4$ concentration (150 mM). (b) Effect of different $NaBH_4$ contents on the HGR of the Co_3B−HEA at a fixed NaOH concentration (0.4 wt%). (c) Curves of the hydrolysis of alkaline $NaBH_4$ solution at different reaction temperatures in the range of 298–318 K. (d) Arrhenius plots of the different catalysts. (e) Reusability test of the Co_3B−HEA catalyst in alkaline $NaBH_4$ solution at 25 °C and (f) the corresponding HGR values in the different cycles. All tests were performed in 150 mM $NaBH_4$ + 0.4 wt% NaOH solution.

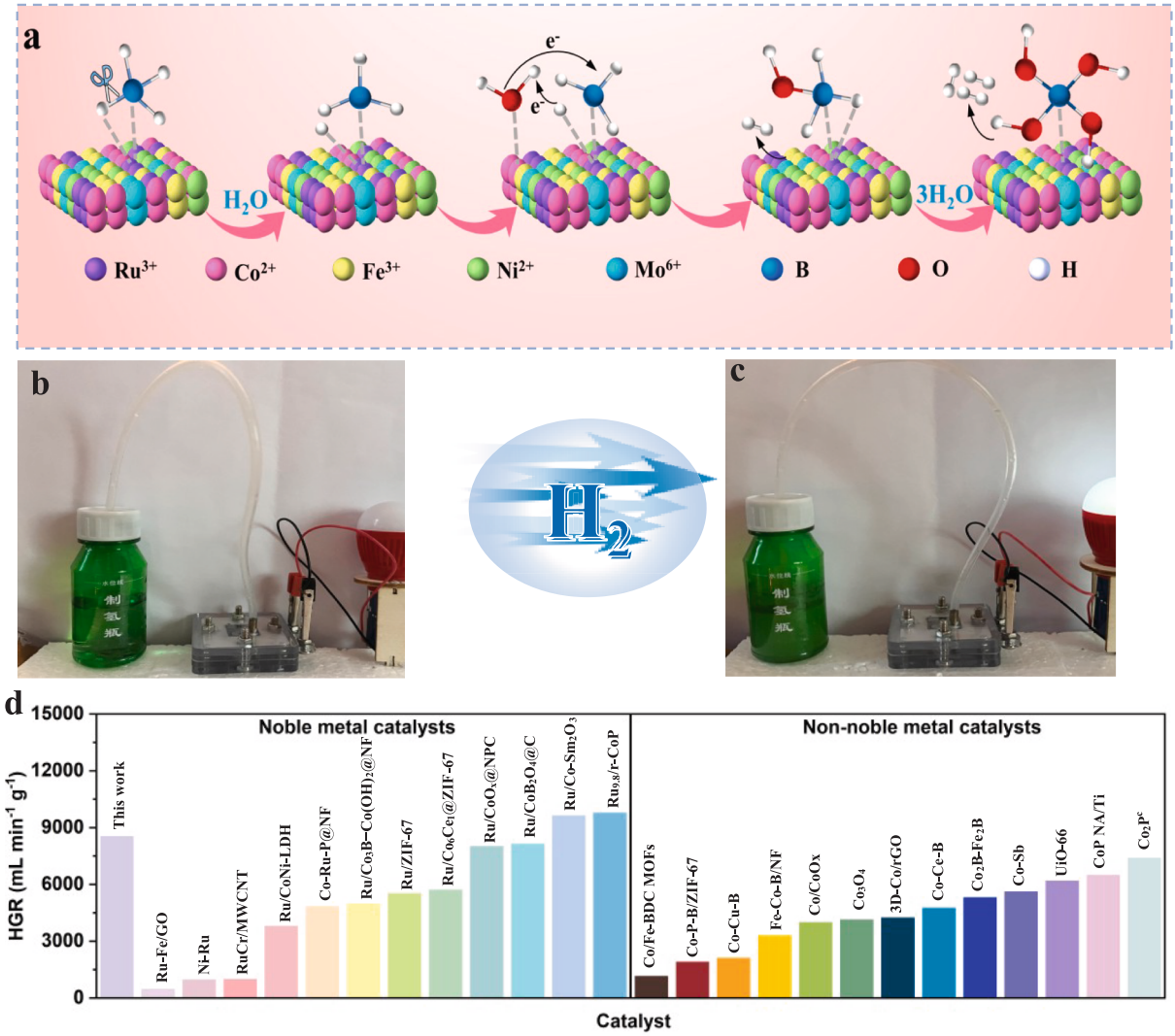

Fig. 7. (a) Proposed mechanism diagram of $NaBH_4$ hydrolysis for H_2 generation. (b-c) Working photo of a light bulb powered by a custom H_2-air fuel cell. (d) Comparison of HGR values for different catalysts (**Table S2**).

negatively charged hydroxide ions (OH^-). This suggests that water molecules preferentially adsorb onto the cobalt species within the catalyst matrix. While $NaBH_4$ dissociates into Na^+ and BH_4^- ions, Intermediate species develop as a result of the BH_4^- anion being attacked by water molecules [62]. Thus, the reaction mechanism can be summarized in the following steps: (I) Adsorption and activation: BH_4^- ions adsorb onto Ru sites on the Co_3B–HEA surface, while H_2O adsorbs onto Co sites. The B–H bond is cleaved, producing adsorbed hydride species ($*H^-$) and an intermediate $*BH_3$; (II) Hydrogen generation: The adsorbed hydride species react with protons derived from water molecules adsorbed at Co sites, releasing H_2 while generating OH^- ions; (III) Intermediate conversion: The remaining OH^- ions interact with the $*BH_3$ species to form BH_3OH^-; (IV) Final hydrolysis: Continued substitution of hydrogen atoms in BH_3OH^- by OH^- results in the formation of tetrahydroxyborate ($B(OH)_4^-$), completing the hydrolysis reaction [63,64].

$$BH_4^- \rightleftharpoons BH_3 + H^- \quad (1)$$

$$H^- + H_2O \rightleftharpoons H_2 + OH^- \quad (2)$$

$$OH^- + BH_3 \rightleftharpoons BH_3OH^- \quad (3)$$

$$OH^- + BH(OH)_3^- \rightleftharpoons B(OH)_4^- + H^- \quad (4)$$

This mechanistic pathway elucidates the role of the Co_3B–HEA catalyst in promoting efficient $NaBH_4$ hydrolysis through the effective adsorption and dissociation of BH_4^- and H_2O molecules. Furthermore, experimental results indicate that the Co_3B–HEA catalyst can generate sufficient hydrogen to power a hydrogen–air fuel cell, as confirmed by the successful illumination of small light bulbs (Figs. 7b and 7c). These findings underscore the catalyst's potential to enhance both hydrogen production efficiency and fuel cell performance. Despite this degradation, the Co_3B–HEA catalyst still demonstrates superior catalytic performance compared to numerous reported noble and non-noble metal-based catalysts, underscoring its significant potential for practical hydrogen generation applications (Fig. 7d and **Table S4**). Furthermore, as shown in **Fig. S17**, the catalyst exhibits excellent magnetic properties, enabling facile magnetic separation and recycling in practical applications.

4. Conclusions

In summary, we have developed an amorphous Co_3B–HEA catalyst that exhibits superior catalytic activity and stability for hydrogen production via $NaBH_4$ hydrolysis under mild alkaline conditions. The enhanced performance stems from the unique amorphous structure and the synergistic interaction between metals, which facilitates electron redistribution, active site exposure, and efficient adsorption and

activation of BH_4^- and H_2O. Based on the reaction process and a number of characterization studies, a trustworthy catalytic mechanism has been suggested. The catalyst continues to outperform the majority of reported non-noble and noble metal-based systems, even when partial metal leaching and by-product buildup reduce activity after several cycles. Furthermore, a tailored H_2–air fuel cell was successfully powered by hydrogen generated by the hydrolysis of $NaBH_4$ catalyzed by the Co_3B–HEA catalyst, proving that it is feasible to transfer chemical energy into electrical energy in a cheap and efficient manner. These results open the door for the logical development of next-generation multimetallic catalytic materials and highlight the potential of HEA-based boride catalysts in realistic hydrogen production.

However, this study still has limitations. First, the hydrothermal-chemical reduction method involves harsh reaction conditions, making large-scale production prone to phase deviation and particle agglomeration due to uneven heat and mass transfer, thus limiting short-term industrial application. Second, the deposition of $NaBO_2$ byproducts and minor metal leaching remain core issues for long-term use. Finally, while the inclusion of trace Ru enhances activity, it increases costs, and the elemental ratios have not been optimized through high-throughput experiments or theoretical calculations. Subsequent efforts will further focus on developing high-entropy materials: First, through "non-metallic doping regulation" (e.g., with B or P elements), optimize the electronic structure of non-precious metals like Co and Fe to compensate for the activity shortcomings of Ru-free systems; second, adopt a "high-entropy dilution strategy" by substituting Ru with trace rare earth elements (e.g., Ce or La) to stabilize active sites via high-entropy effects. Third, developing "catalyst recycling processes" to recover Ru from spent catalysts via acid leaching-recrystallization, thereby reducing resource consumption.

CRediT authorship contribution statement

Huaxia Zhou: Writing – original draft, Data curation, Conceptualization. **Chenxi Shang:** Formal analysis, Conceptualization. **Tayirjan Taylor Isimjan:** Visualization, Validation, Supervision. **Xiulin Yang:** Writing – review & editing, Supervision, Funding acquisition.

Declaration of competing interest

The authors declare that they have no known competing financial interests or personal relationships that could have appeared to influence the work reported in this paper.

Acknowledgements

This work has been supported by the National Natural Science Foundation of China (no. 52363028, 21965005), the Natural Science Foundation of Guangxi Province (2021GXNSFAA076001 and 2018GXNSFAA294077), and the Guangxi Technology Base and Talent Subject (GUIKE AD23023004 and GUIKE AD20297039).

Appendix A. Supplementary data

Supplementary data to this article can be found online at https://doi.org/10.1016/j.fuel.2026.138521.

Data availability

The data that has been used is confidential.

References

[1] Qiu H-J, Fang G, Wen Y, Liu P, Xie G, Liu X, et al. Nanoporous high-entropy alloys for highly stable and efficient catalysts. J Mater Chem A 2019;7:6499–506.
[2] Pedersen JK, Batchelor TAA, Bagger A, Rossmeisl J. High-Entropy Alloys as Catalysts for the CO_2 and CO Reduction Reactions. ACS Catal 2020;10:2169–76.
[3] Lv ZY, Liu XJ, Jia B, Wang H, Wu Y, Lu ZP. Development of a novel high-entropy alloy with eminent efficiency of degrading azo dye solutions. Sci Rep 2016;6:34213.
[4] Wang Y, Zheng X, Wang Y, Li X, Liu Y, Xia Z. Effect of loaded Co–B on hydrogen release performance of sodium borohydride. J Phys Chem Solid 2025;204:112761.
[5] Tran DT, Van HT, Nguyen LH, Van Quang N, Tsai Y-C, Lin K-Y-A, et al. Hierarchical porous cobalt nanoparticles encapsulated in heteroatom-doped hollow carbon as an enhancing multifunctional catalyst for hydrolysis of sodium borohydride and hydrogenation of bromate in water. Surf Interfaces 2024;48:104329.
[6] Yurderi M. PtCo/g-C_3N_4 bimetallic catalyst: Boosting hydrogen production in sodium borohydride hydrolysis. Int J Hydrogen Energy 2025;143:105–11.
[7] Zhou S, Cheng L, Liu Y, Tian J, Niu C, Li W, et al. Highly active and Robust Catalyst: Co_2B–Fe_2B Heterostructural Nanosheets with Abundant Defects for Hydrogen Production. Inorg Chem 2024;63:2015–23.
[8] Zhou S, Yang Q, Liu Y, Cheng L, Taylor Isimjan T, Tian J, et al. Electronic metal-support interactions for defect-induced Ru/Co-Sm_2O_3 mesosphere to achieve efficient $NaBH_4$ hydrolysis activity. J Catal 2024;433:115491.
[9] Mirshafiee F, Rezaei M. Enhancing hydrogen generation from sodium borohydride hydrolysis and the role of a Co/$CuFe_2O_4$ nanocatalyst in a continuous flow system. Sci Rep 2024;14:9659.
[10] Chu F, He J, Wang J, Lei N, Yuan S, Zhang S, et al. Medium-entropy alloy design enables highly efficient catalytic methanolysis of ammonia borane. Applied Catalysis B: Environment and Energy 2025;368:125140.
[11] Lin C-Y, He ZY, Lin J-T, Chang C-W, Hsiao Y-C, Lin S-C, et al. Atomically mixed High-Entropy-Alloy Nanoframes with 3D Subnanometer-Thick Electrocatalytic Surfaces. Adv Funct Mater 2025;35:2505927.
[12] Jing Z, Guo Y, Wang Q, Yan X, Yue G, Li Z, et al. Ambient hydrogenation of solid aromatics enabled by a high entropy alloy nanocatalyst. Nat Commun 2024;15:5806.
[13] Wu D, Kusada K, Nanba Y, Koyama M, Yamamoto T, Toriyama T, et al. Noble-Metal High-Entropy-Alloy Nanoparticles: Atomic-Level Insight into the Electronic Structure. J Am Chem Soc 2022;144:3365–9.
[14] Chen ZW, Li J, Ou P, Huang JE, Wen Z, Chen L, et al. Unusual Sabatier principle on high entropy alloy catalysts for hydrogen evolution reactions. Nat Commun 2024;15:359.
[15] C.-Y. Wu, Y.-C. Hsiao, Y. Chen, K.-H. Lin, T.-J. Lee, C.-C. Chi, J.-T. Lin, L.-C. Hsu, H.-J. Tsai, J.-Q. Gao, C.-W. Chang, I.T. Kao, C.-Y. Wu, Y.-R. Lu, C.-W. Pao, S.-F. Hung, M.-Y. Lu, S. Zhou, T.-H. Yang, A catalyst family of high-entropy alloy atomic layers with square atomic arrangements comprising iron- and platinum-group metals, Sci. Adv. 10 eadl3693.
[16] Guan S, Yuan Z, Zhao S, Zhuang Z, Zhang H, Shen R, et al. Efficient Hydrogen Generation from Ammonia Borane Hydrolysis on a Tandem Ruthenium–Platinum–Titanium Catalyst. Angew Chem Int Ed 2024;63:e202408193.
[17] Chu H, Li G, Liu C, Cui C, Li Y, Qiu S, et al. Ruthenium-based High-Entropy Alloys Expediting Hydrogen Evolution through Catalytic Hydrolysis of Ammonia Borane. ACS Appl Energy Mater 2024;7:9625–33.
[18] Jin S, Li Y, Yang Y, Zhang W. Novel nanoporous amorphous/nanocrystalline composite structured RuNiFeCo multicomponent alloys with exceptional catalytic activity for ammonia borane hydrolytic dehydrogenation. Mater Today Nano 2024;26:100485.
[19] Wei R, Zhang K, Zhao P, An Y, Tang C, Chen C, et al. Defect-rich FeCoNiPB/$(FeCoNi)_3O_4$-x high-entropy composite nanoparticles for oxygen evolution reaction: Impact of surface activation. Appl Surf Sci 2021;549:149327.
[20] Luo C, Wang W-N, Qiao M-H, Fan K-N. Adsorption of sulfur on Ni_mB_2 clusters: a theoretical investigation on the mechanism of strong sulfur resistance of Ni–B alloy catalyst. J Mol Catal A Chem 2002;184:379–86.
[21] Hu T-H, Wu C-Y, He ZY, Chen Y, Hsu L-C, Pao C-W, et al. Unconventional Hexagonal Close-Packed High-Entropy Alloy Surfaces Synergistically Accelerate Alkaline Hydrogen Evolution. Adv Sci 2025;12:2409023.
[22] Duan C, Liang K, Zhang Z, Li J, Chen T, Lv D, et al. Recent advances in the synthesis of nanoscale hierarchically porous metal–organic frameworks. Nano Mater Sci 2022;4:351–65.
[23] Wang Z, Yang P, Liu D, Jin W, Xiao W, Xiao Z, et al. Amorphous Ru coupled with Defect-Abundant B-Doped FeP_4/Fe_2P Porous Nanospheres as an Electrocatalyst for Hydrogen Generation with a Wide pH Range. ACS Appl Nano Mater 2023;6:19905–14.
[24] Wang X, Jiang G, Wu D, Feng Y. Preparation and growth mechanism of $YFeO_3$ magneto optic crystals. Ceram Int 2024;50:2600–10.
[25] Zhai Y, Ren X, Yan J, Liu S. High Density and unit activity Integrated in Amorphous Catalysts for Electrochemical Water Splitting. Small Struct 2021;2:2000096.
[26] Wang A-L, Xu H, Li G-R. NiCoFe Layered Triple Hydroxides with Porous Structures as High-Performance Electrocatalysts for overall Water Splitting. ACS Energy Lett 2016;1:445–53.
[27] Fan L, Ji Y, Wang G, Chen J, Chen K, Liu X, et al. High Entropy Alloy Electrocatalytic Electrode toward Alkaline Glycerol Valorization Coupling with Acidic Hydrogen Production. J Am Chem Soc 2022;144:7224–35.
[28] Zou Y, Zhao H, Zhang W-D, Gong Q, Liu J, Yang X, et al. High entropy alloy supported ruthenium single-atoms for enhanced electrochemical hydrogen evolution reaction. Chem Eng J 2025;518:164784.
[29] Sui Q, Guo Y, Xiang C, Wang Q, Luo Y, Sun L, et al. Room temperature boronized and phosphated cobalt-nickel metal-organic framework as the electrode material for supercapacitors. J Storage Mater 2022;51:104372.

[30] Shang C, Lu B, Wu C, Zhou S, Shi L, Isimjan TT, et al. Inducing electronic rearrangement through Co_3B-Mo_2B_5 catalysts: Efficient dual-function catalysis for $NaBH_4$ hydrolysis and 4-nitrophenol reduction. Chin Chem Lett 2025;111152.
[31] Hsiao Y-C, Wu C-Y, Lee C-H, Huang W-Y, Thang HV, Chi C-C, et al. A Library of Seed@High-Entropy-Alloy Core–shell Nanocrystals with Controlled Facets for Catalysis. Adv Mater 2025;37:2411464.
[32] Döleker KM, Günen A, Erdoğan A. Boriding influence on cyclic oxidation of CrFeMnNbNi high entropy alloy. Surf Coat Technol 2025;495:131564.
[33] Cengiz S, Azakli Y, Ceylan D, Tarakci G, Tarakci M, Gencer Y, et al. Effects of Nb on borosiliciding of CoCrFeNiNbx high-entropy alloy. Vacuum 2023;207:111677.
[34] Hu Y, Guo M, Hu C, Dong J, Yan P, Taylor Isimjan T, et al. Engineering cobalt nitride nanosheet arrays with rich nitrogen defects as a bifunctional robust oxygen electrocatalyst in rechargeable Zn–air batteries. J Colloid Interface Sci 2022;608:2066–74.
[35] Onat E, Ekinci S, Izgi MS, Erkan E, Atiç S, Kocaman B, et al. Sustainable hydrogen production from $NaBH_4$ using Co@CHE Catalyst: Experimental and MLP-Based modeling for autonomous fuel systems. Fuel 2026;406:136999.
[36] Onat E, Horoz S, Şahin Ö, İzgi MS. Revolutionary carbon quantum dot supported-Co catalyst for record-breaking hydrogen production rate. J Aust Ceram Soc 2025;61:117–26.
[37] Song J-W, Fan L-W. Temperature dependence of the contact angle of water: a review of research progress, theoretical understanding, and implications for boiling heat transfer. Adv Colloid Interface Sci 2021;288:102339.
[38] Luo Y, Xia Y, Zhou H, Yin C, Yang H, Chen J, et al. Effect of calcium ions on surface properties of chalcopyrite and arsenopyrite and its response to flotation separation under low-alkalinity conditions. Appl Surf Sci 2022;602:154191.
[39] Ma J, Zhu Y, Huang K, Wang P, Liu D, Zhao Y. High-entropy alloy catalysts of FeCoNiCuMo/C with high stability for efficient oxygen evolution reaction. J Alloy Compd 2024;997:174922.
[40] Zhou S, Jang H, Qin Q, Hou L, Kim MG, Liu S, et al. Boosting Hydrogen Evolution Reaction by phase Engineering and Phosphorus Doping on Ru/P-TiO_2. Angew Chem Int Ed 2022;61:e202212196.
[41] Hung K-M, Wu J-J. Bifunctional nickel phosphide nanoparticle/nickel cobalt sulfide nanosheet framework for electrocatalytic simultaneous hydrogen evolution and 2,5-Furandicaroxylic acid production. Chem Eng J 2024;484:149772.
[42] Onat E, Izgi MS, Şahin Ö, Saka C. Robust carbon quantum dots supported cobalt oxide composite particles prepared by hydrothermal process for green hydrogen generation via sodium borohydride hydrolysis. Fuel 2024;378:132900.
[43] Jiang R, Shi Z, Zhao W, Gao B, Wu T, Yuan Q. Vacancy-Assisted Growth Mechanism of Multilayer Hexagonal Boron Nitride on a Fe_2B Substrate. J Phys Chem Lett 2020;11:8511–7.
[44] Liu Q, Zhao H, Jiang M, Kang Q, Zhou W, Wang P, et al. Boron enhances oxygen evolution reaction activity over Ni foam-supported iron boride nanowires. J Mater Chem A 2020;8:13638–45.
[45] Gao Z, Yu ZW, Liu FQ, Yu Y, Su XM, Wang L, et al. Ultralow-Content Iron-decorated Ni-MOF-74 Fabricated by a Metal–Organic Framework Surface Reaction for Efficient Electrocatalytic Water Oxidation. Inorg Chem 2019;58:11500–7.
[46] Zhuang DW, Kang Q, Muir SS, Yao XD, Dai HB, Ma GL, et al. Evaluation of a cobalt-molybdenum-boron catalyst for hydrogen generation of alkaline sodium borohydride solution-aluminum powder system. J Power Sources 2013;224:304–11.
[47] Xu X, Guo Y, Bloom BP, Wei J, Li H, Li H, et al. Elemental Core Level Shift in High Entropy Alloy Nanoparticles via X-ray Photoelectron Spectroscopy Analysis and First-Principles Calculation. ACS Nano 2020;14:17704–12.
[48] Hao J, Zhuang Z, Cao K, Gao G, Wang C, Lai F, et al. Unraveling the electronegativity-dominated intermediate adsorption on high-entropy alloy electrocatalysts. Nat Commun 2022;13:2662.
[49] Tian X, Li H, Chang R, Yang Y, Wang Z, Dong T, et al. Rapid, self-sacrificing template synthesis of two dimensional high-entropy oxides toward high-performance oxygen evolution. J Mater Chem A 2024;12:3276–82.
[50] Kang J, Qiu X, Hu Q, Zhong J, Gao X, Huang R, et al. Valence oscillation and dynamic active sites in monolayer NiCo hydroxides for water oxidation. Nat Catal 2021;4:1050–8.
[51] Feng D, Dong Y, Nie P, Zhang L, Qiao Z-A. CoNiCuMgZn high entropy alloy nanoparticles embedded onto graphene sheets via anchoring and alloying strategy as efficient electrocatalysts for hydrogen evolution reaction. Chem Eng J 2022;430:132883.
[52] Deonikar VG, Rajkamal A, Kim H. 3D hollow microrod engineered MOF-derived Cu/Co catalysts promoted by Al nanoflakes for efficient H_2 generation through $NaBH_4$ hydrolysis: Perceptions on boosted reaction channels aided by a synergistic effect. Sustainable Mater Technol 2023;38:e00711.
[53] Li H, Hu X, Wang L, Shi L, Isimjan TT, Yang X. Kinetically promoted hydrogen generation by Ru nanoparticles decorated CoB_2O_4 on mesoporous carbon spheres with rich oxygen vacancies for $NaBH_4$ hydrolysis. Chem Eng J 2024;481:148547.
[54] Liu S, He Y, Cheng Q, Huan Y, Yuan X, Liu J, et al. Triggering Heteroatom Ensemble effect over RuFe Alloy to Promote Nitrogen Chemisorption for Efficient Ammonia Electrosynthesis at Ambient Conditions. J Phys Chem Lett 2024;15:8990–6.
[55] Zhang X, Li Z, Sun X, Wei L, Niu H, Chen S, et al. Regulating the Surface Electronic Structure of RuNi Alloys for Boosting Alkaline Hydrogen Oxidation Electrocatalysis. ACS Mater Lett 2022;4:2097–105.
[56] Shang C, Shi L, Zhou S, Muhammad S, Isimjan TT, Hu H, et al. Interface engineering of Co_2B–MoO_3/MOF heterojunctions with rich cobalt defects for highly enhanced $NaBH_4$ hydrolysis. Inorg Chem Front 2024;11:7142–51.
[57] Zhang J, Lin F, Yang L, He Z, Huang X, Zhang D, et al. Ultrasmall Ru nanoparticles supported on chitin nanofibers for hydrogen production from $NaBH_4$ hydrolysis. Chin Chem Lett 2020;31:2019–22.
[58] Onat E, Ekinci S, Şahin Ö, İzgi MS. Effective and environmentally friendly Co nanocatalyst on sodium borohydride hydrolysis in different solvents. Int J Hydrogen Energy 2025;142:864–74.
[59] Zhou S, Cheng L, Huang Y, Liu Y, Shi L, Isimjan TT, et al. Constructing Ru particles decorated Co_3B-CoP heterostructures as a highly active and reusable catalyst for H_2 generation by catalyzing $NaBH_4$ hydrolysis. Appl Catal B 2023;328:122519.
[60] Izgi MS, Şahin Ö, Faal S, Celik FA, Onat E, Karabulut E. Green synthesis of highly efficient and stable Ni@CQD nanoparticles: Experimental and theoretical approach for hydrogen production from dimethyl aminborane and sodium borohydride hydrolysis. Fuel 2025;397:135412.
[61] Onat E, Alan Y, Savcı A, Ekinci S, İzgi MS. Green-synthesized Co@VHE nanocatalyst from Verbascum insulare for enhanced hydrogen generation and biological applications. Biomass Bioenergy 2026;204:108435.
[62] Onat E, İzgi MS, Şahin Ö, Ekinci S. Enhanced hydrogen production from sucrose-derived carbon quantum dots-supported Ru catalysts: a comparative study of KBH_4 and $NaBH_4$ hydrolysis. Renew Energy 2025;254:123692.
[63] Onat E. Synthesis of a cobalt catalyst supported by graphene oxide modified perlite and its application on the hydrolysis of sodium borohydride. Synth Met 2024;306:117621.
[64] Rathod S, Gajjar D, Joshi KK, Pataniya P, Sumesh CK, Kapatel S. Catalytic hydrogen production via $NaBH_4$ hydrolysis: Role of WO_3 nanopellets. Renew Energy 2025;248:123156.